EFFECT OF NONMETALLIC INCLUSIONS ON SOLIDIFICATION OF INOCULATED SPHEROIDAL GRAPHITE IRON

Simon N. Lekakh
Missouri University of Science and Technology, Rolla, MO, USA

https://doi.org/10.1007/s40962-018-0243-2

Abstract

Inoculation treatment of spheroidal graphite cast iron (SGI) controls graphite nodule heterogeneous nucleation and is used for elimination of solidification microporosity and improvement in casting performance. In this study, thermodynamic simulations were performed to predict precipitates formed in the inoculated melt above a liquidus temperature (primary precipitates) and during solidification (secondary precipitates). The experimental inoculation treatments were designed targeting formation of primary precipitates (Ti and Zr additions) and secondary precipitates (S and N additions to inoculant). An automated SEM/EDX analysis was applied to analyze the graphite nodule distribution statistics and a family of nonmetallic inclusions in the experimental castings. In inoculated SGI, the observed bimodal distributions of graphite nodules were related to continuous nucleation with the second nucleation wave that occurred toward the solidification end. The measured microporosity in the castings was linked to graphite nucleation. The origin of the continuous graphite nodule nucleation and the possibility of engineering nonmetallic inclusions to control casting soundness are discussed.

Keywords: *cast iron with spheroidal graphite, solidification, inoculation, nonmetallic inclusions*

Literature Review

Micro-Defects in SGI Castings Originated During Solidification

Microstructural inconsistencies, including variations in graphite shape, alloying elements segregation, microporosity, as well as macro-imperfections, such as cracks, are created during solidification of spheroidal graphite cast iron (SGI). Therefore, control of graphite nodule precipitation during solidification is used to eliminate these imperfections and improve the overall casting performance. Among these imperfections, microporosity in SGI castings is a critical defect. Kainzinger et al.[1] demonstrated that microporosity is a dominant reason for crack initiation during SGI fatigue tests of machined specimens.

It is well known that precipitation of a low-density graphite phase directly from the melt increases a specific volume of Fe–C–Si alloys. Such volume increase could compensate a total thermal shrinkage and partially or fully eliminate shrinkage defects in SGI castings. Graphite precipitation in the casting develops a solidification pressure on the mold wall; however, casting geometry changes depend on a combination of intrinsic (solidification kinetics, graphite shape, mushy zone structure) and extrinsic (rate of heat extraction, mold rigidity, external risering) factors. Mampaey showed a marked difference in mushy zone structure between lamellar and spheroidal graphite cast iron.[2] The experimental results show that lamellar graphite cast iron solidifies with the formation of tight solid skin. This is not the case in SGI, which solidifies in a very mushy way so that a continuous liquid phase remains in contact with the mold wall for a relatively long period during solidification. Alonso et al.[3] showed that changing lamellar to compacted and spherical graphite shape by adding magnesium increased the amount and the time of linear expansion in these cast irons with similar carbon equivalent. Low linear expansion in cast iron with flake graphite (GI) is related to development of a solid shell followed by a narrow mushy zone during early solidification stage. This solidification mode in GI prevents deformation of casting surface when compared to SGI which solidified with a soft and extended mushy zone. Such changes in the mushy zone structure provide a difference in shrinkage defect tendency in SGI when compared to GI.

Microporosity formed in castings has been linked to the mushy zone structure in different alloys. Typically, grain refinement by melt inoculation extends the mushy zone in eutectic type alloys. Therefore, inoculation could facilitate microporosity in the alloys where the precipitated solid phases have higher density than the melt. Knuutinen et al.[4] demonstrated this relationship in grain refined aluminum alloys. In SGI, graphite nodule inoculation also extends the mushy zone; however, Skaland [5] showed that an effective inoculation decreases sensitivity to form microporosity. Solvo et al.[6] also reported that inoculation is detrimental to SGI casting soundness because of increased numbers of graphite nodules.

Graphite precipitation from the melt causes a volume increase during the solidification; therefore, control of the kinetics of graphite eutectic solidification could be used as an effective way to eliminate shrinkage microporosity. Let us consider two solidification scenarios: (i) early instantaneous graphite nodule nucleation at maximal undercooling and (ii) continuous graphite nodule nucleation toward the end of solidification. The first solidification mode a priori assumes that the potential heterogeneous nucleation sites already existed in the melt before solidification started. In this solidification scenario, the casting volume increase caused by massive graphite growth on the early solidification stage will provide pressure on mold/casting interface and the soft casting surface could swell in the flexible. The following decrease in melt volume at the end of solidification is not compensated because developed solid network blockades direct feeding of isolated melt pockets and microporosity will be formed. Lesoult[7] discussed three main causes of microporosity formation in SGI at solidification end, i.e., local chemistry of liquid, local dendritic microstructure, and local liquid pressure within the mushy zone.

The second scenario assumes the continuous nucleation and growth of graphite nodules to the end of solidification. This scenario could promote decreasing microporosity. In the ideal case, this solidification mode could help self-healing of shrinkage in a casting solidified without a riser. The technical possibility to realize a second scenario by effective melt inoculation and increasing mold rigidity was experimentally confirmed in SGI by many authors. Chisamera et al.[8] found that the FeSi inoculation with Ce, Ca, S and O additions provided a specific bimodal graphite nodule size distribution. In this case, nodule diameter distribution curve consisted of two overlapped sets of relatively large nodules formed at the start of solidification and smaller nodules formed later toward the end of solidification. Pederson et al.[9] and the authors[10] observed non-uniform graphite nodule distributions in well inoculated SGI. Recently, Yin et al.[11] directly observed two categories of graphite nodules using 3D X-ray micro-tomography, which were classified as precipitated in eutectic cell (large diameter) and located between cells (small diameter).

Determination of Solidification Kinetics in SGI Casting

Described SGI solidification scenarios assumed the different graphite nodules nucleation modes, and it is important to have supporting experimental results. Two-dimensional X-ray radiography with micron-scale spatial resolution was recently used by Yamane et al.[12] for visualization of the solidification kinetics in very thin X-ray transparent specimens from SGI. However, direct observation of graphite nodule precipitation in the real castings with such resolution is not technically feasible today. An interrupted solidification technique provides information about a mushy zone structure,[2] but a limited cooling rate does not prevent precipitation of small graphite nodules during quenching. Several indirect experimental methods assisted by simulations have been developed to reconstruct the solidification kinetics in the casting. Dioszegi et al.[13] used an inverse kinetic analysis to study eutectic growth by simulation of the cooling curve and fitting it to the experimentally measured cooling curve in the casting. The results indicated that this method can accurately back-calculate the overall evolution of the solid fraction during casting solidification. However, this approach is not sufficiently sensitive to predict a second nucleation wave of graphite nodules because it will have a relatively small effect on the cooling curve shape. Bhaskaran et al.[14] tried to correlate the parameters extracted from the cooling curves with observed microporosity in the castings, but the strong correlations were not determined. Larranaga et al.[15] collected 600 cases, and advanced computer-aided thermal analysis was applied for the evaluation of shrinkage propensity and to link it to the cooling curve parameters, total nodule count and the measured linear contraction. Stefanescu et al.[16] used combined measurements of the linear contraction and the cooling curve to better understand the shrinkage phenomenon, and they stated that further work is necessary to analyze the differences in solidification mechanisms of cast irons with different graphite shapes. When compared to direct observation of solidification in tiny specimen, these indirect methods have some advantages because they investigate solidification processes in a whole casting.

However, these indirect methods struggle to deliver the real solidification kinetics. The author[17,18] suggested an indirect method for structural reconstruction of the nucleation kinetics in the SGI casting based on analysis of the final 3D graphite nodule diameter distribution after solidification. This method assumes that the final 3D distribution of graphite nodules mirrored a casting solidification sequence, because the majority of early formed nodules have time to grow while graphite nodules formed at the solidification end will be small. Therefore, it is possible to reconstruct a relative sequence of graphite nodule nucleation events from the nodule diameter distribution in the final casting

structure. The structural reconstruction method has limitations because it needs a priori assumptions about space distribution of nuclei and growth kinetics. The suggested computational algorithm[17,18] assumes ordered distribution of transient (time dependent) nuclei in the melt and two-stage graphite nodule growth model: linear free growth in the melt and parabolic declined growth in the austenite envelop. The conversion limitation of inverse simulated structure did not allow one to implement into a model a stochastic distribution of nuclei in the melt. A random distribution of near neighboring distances will generate more small nodules when compared to an ordered distribution. The real nucleation processes are between these two extreme cases. The applied limitation resulted in some distortion of the shape of reconstructed nucleation rate curve; therefore, the results were used for relative comparison of different inoculation practices.

In this article, the thermodynamic simulations were used to predict the formation sequence of non-metallic inclusions and its composition in inoculated SGI. An automated SEM/EDX analysis was performed for determination of the family of non-metallic inclusions, graphite nodule distribution and reconstructed nucleation kinetics. The effect of SGI processing on porosity in experimental castings was determined and the principles of engineering non-metallic inclusions to increase casting performance were discussed.

Methods

Thermodynamic Simulations of Potential Heterogeneous Nuclei

A classical approach assumes instantaneous heterogeneous nucleation of graphite nodules at maximal undercooling on the ready randomly distributed primary heterogeneous nucleation sites in the melt. Theoretically, this mode will provide a near log-normal distribution of 3D diameters of cast grains. However, the experimental data[8–10] indicate about more complicated graphite nodule distribution in inoculated SGI castings, which could be related to the continuous nucleation toward the end of solidification and a possible second nucleation wave. The second nucleation wave could be initiated again by the small primary heterogeneous nuclei because of high undercooling at the end of solidification[19] and also as results of forming a new active precipitates. This means that a family of heterogeneous nuclei could be changed during solidification by developing the new or "secondary" active nucleation sites during solidification process. There are several possible transient or process time-dependent thermodynamic conditions for forming the secondary nonmetallic inclusions during solidification, which included: (i) segregation of the active elements on solidification front and (ii) increasing the affinity of the active elements in the melt to form the fresh compounds with decreasing temperature. Recently, Muhmond et al. studied the effect of Mg segregation during SGI solidification on forming secondary oxides and sulfides.[20]

A chemically assisted formation of the potential heterogeneous nucleation sites during SGI processing was analyzed in this article. Thermodynamic FACTSAGE software[21] was used to simulate the possible irreversible chemical reactions in the Mg-treated and inoculated near eutectic Fe–Si–C alloy (3.6 wt%C, 2.5 wt%Si, 0.03 wt%Mg). After each melt treatment stage, the reaction products were "extracted" and the melt proceeded to cooling and solidification with step-by-step simulation of thermodynamic equilibrium in mushy zone. Simulations were done for restricted number of steps. The list of studied additions to inoculant included: (i) the electropositive transitional metals (Zr and Ti) available react with remained dissolved metalloid impurities (O, N) after Mg treatment and (ii) the electronegative elements (S and N) available react with dissolved Mg.

Thermodynamic simulations predicted three classes of precipitates related to different conditions of formation during SGI processing (Figure 1a):

- *Primary* precipitates formed in the melt above the liquidus temperature: (i) developed during Mg treatment (mainly Mg and RE oxides and sulfides) and (ii) formed during inoculation treatment. For example, the Zr and Ti additions with inoculant can react with nitrogen dissolved in Mg-treated melt and form primary nitrides;
- *Secondary* precipitates, which will be formed below the liquidus temperature in the mushy zone. This category of precipitates includes Mg nitrides. Increasing affinity of N to Mg and lowering temperature together with a positive segregation of these elements into the melt will promote the secondary nitrides formation during solidification. Solberg and Onsoien found complex nitride inside graphite nodules, identified as $AlMg_{2.5}Si_{2.5}N_6$ having a trigonal superlattice. Also, Ti–Mg ratio defines a composition of nitrides formed in the mushy zone (Figure 1b);
- *Mixture* of primary and secondary precipitates. For example, part of sulfides will be immediately formed in the melt inoculated with S additions by reaction with dissolved Mg, Ca, La or Ce. Two mechanisms could promote formation of a small portion of the secondary sulfides during solidification by: (i) rejection of C and S into the remaining melt by growing austenite dendrites, which will significantly increase sulfur activity, and (ii) increasing thermodynamic stability of sulfides with lowering temperature at solidification end.

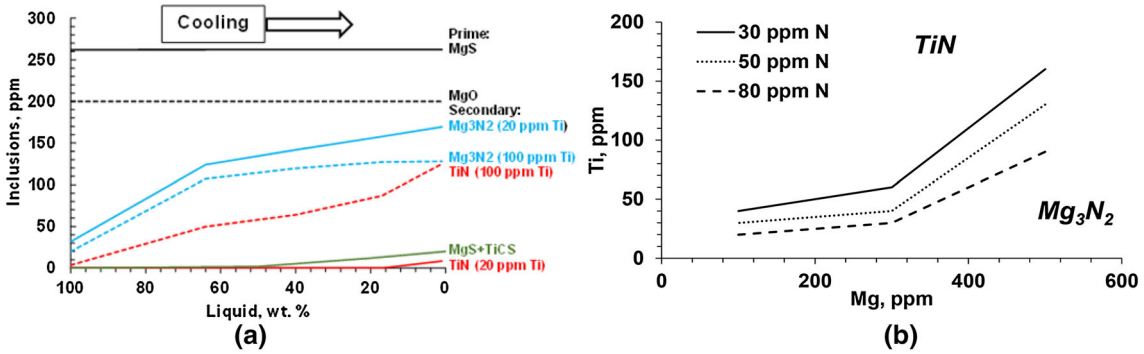

Figure 1. Sequence of primary and secondary precipitations in the melt (50 ppm N) upon cooling and solidification (a) and equilibrium between TiN and Mg_3N_2 in mushy zone at different Ti and N levels (b).

The amount of secondary sulfide and nitride precipitates (color lines in Figure 1a) increases during solidification, and they will be formed by the co-precipitation mechanism in the melt prime inclusions. Such complex compounds were observed inside graphite nodules in many cases mentioned in review.[23] A high-resolution transmission electron microscopy research[22] and an SEM/EDX analysis[23,24] found different types of nonmetallic inclusions in SGI; however, used in this study FactSage thermodynamic databases do not have data on such complex inclusions as Mg–Si–Al nitrides, which were found inside nodules,[21] and described calculations predicted mainly pure substances. The predictions followed from this thermodynamic analysis were used to design the active at hundred ppm level additions of S, N, Ti or Zr to control nucleation kinetics through changing a formation sequence of the potential nucleation sites for graphite nodules.

Experimental Heats

The experimental trials were performed to verify the possibility of controlling solidification kinetics by inoculation, applying a commercial complex inoculant (74Si, 1.1Al, 1.1Ca, 0.8Ba, in wt%) with additions of S, N, Ti or Zr. These additions were designed using thermodynamic simulations. SGI was prepared in a 200-lb induction furnace by melting an industrial purity metallic charge consisting of 50 wt% induction iron and 50 wt% industrial ductile iron revert. The melt was treated in a 200-lb ladle by commercial FeSiMg alloy (in wt%) (45.4Si, 4.03Mg, 0.44La, 0.97Ce, 0.75Al). After that, SGI was poured into several 25-lb handle ladles with 0.3 wt% commercial inoculant without and with additions of S, N, Ti or Zr. The test articles 100 × 200 × 16 mm (4″ × 8″ × 0.6″) horizontal plates with three top cylindrical bosses of different diameters (17, 22 and 28 mm or 0.65″, 0.86″ and 1.1″) to observe micro-shrinkage forming tendency were poured at 1340–1350 °C using non-bake molds. The chemistry of SGI is given in Table 1. The samples for microstructure analysis were taken from the flat part of the plates. The specimens for microporosity were cut from medium-size bosses using core drill. Microporosity was determined by Archimedes method, comparing plates and bosses densities.

Nonmetallic Inclusion Analysis and Structural Reconstruction of Nucleation Kinetics

An automated SEM/EDX analysis (ASPEX) was used to collect the "true" families of 2D graphite nodule diameter and metallic inclusions. Briefly, the several thousand features were detected and measured during SEM backscattered electron detector imaging from each SGI using brightness contrast threshold from the matrix. Simultaneously performed EDX analysis of each feature was used to separate graphite phase from inclusions. This procedure counted mainly inclusions in the metal matrix because low probability to detect small (micron size) inclusions on the middle of 10–50 microns nodules. An example of a map of nonmetallic inclusions and graphite nodules distribution in random 2D section is shown in Figure 2a. A joint ternary diagram of nonmetallic inclusions was built using methodology suggested by Harris et al.,[25] and statistics of 2D particles with differentiation of graphite from nonmetallic inclusions is illustrated in Figure 2b. To detect inclusions inside graphite nuclei, the second automated

Table 1. Chemistry of Experimental SGI (wt%)

C	Si	Mn	Cr	Cu	Ni	Mg	S	N	O
3.63	2.4	0.15	0.05	0.05	0.02	0.045	0.004	0.005	0.01

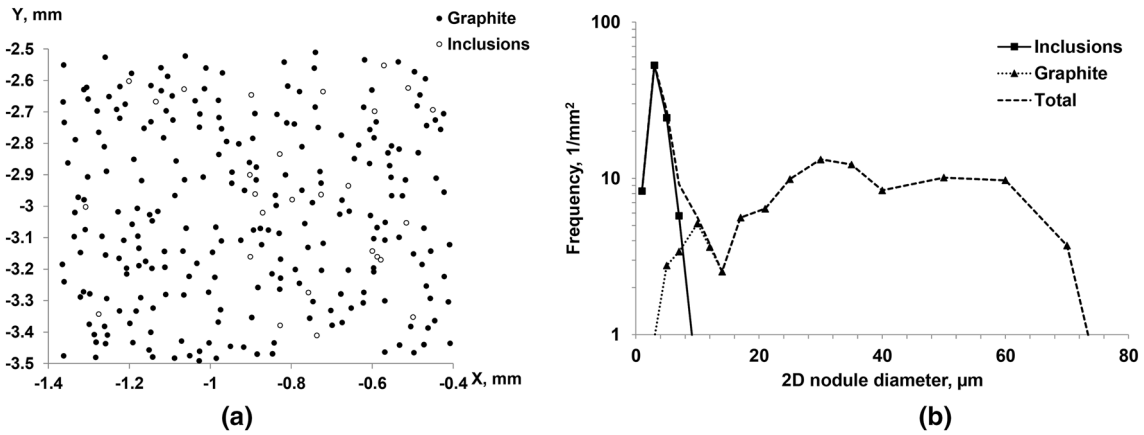

Figure 2. Example of an automated SEM/EDX analysis of micro-features in SGI structure: (a) map of all detected features and (b) 2D particle diameter distributions.

SEM/EDX analysis was performed by thresholding only graphite nodules and applying extended search of approximately 10,000 nodules.

This analysis resulted in collecting the "clean" 2D distributions of graphite nodule circles in the polished casting section, which then were used to perform a 3D conversion with the method suggested by the authors.[10] To verify this methodology, one SGI sample was electrolytically dissolved, the graphite nodules were filtered, their real 3D diameters were measured using SEM and the results were compared to 2D/3D conversion (Figure 3).

A method for the reconstruction of the solidification kinetics based on analysis of a final graphite nodule distribution in the SGI castings was used.[17,18] The EXCEL built integrator generates an arbitrary number of new graphite nodules in the remaining melt at each solidification step. 20 steps were used in this study. These nodules could grow with velocity ($v = dr/d\tau$) according to a two-step growth model: initial fast growth in the melt with constant velocity until $D_{critical} < 5$ μm and after that parabolic decline graphite nodule growth inside an austenite shell. The numerical parameters of the time-dependent nucleation and growth were determined by inverse simulation with fitting simulated and experimental structures. From these simulations, the relative nucleation rate in 1 mm^3 volume was determined as a number of nucleated nodules at a time period equal to 1/20 solidification period. The integrator determined the time-dependent rates of nucleation and nodule growth in a virtual SGI, which will "solidify" with a structure similar to that, which was experimentally observed in a particular casting volume. Considering the limitations described of the used algorithm, the reconstructed relative nucleation rate was used only to compare relative trends observed in different inoculation scenarios.

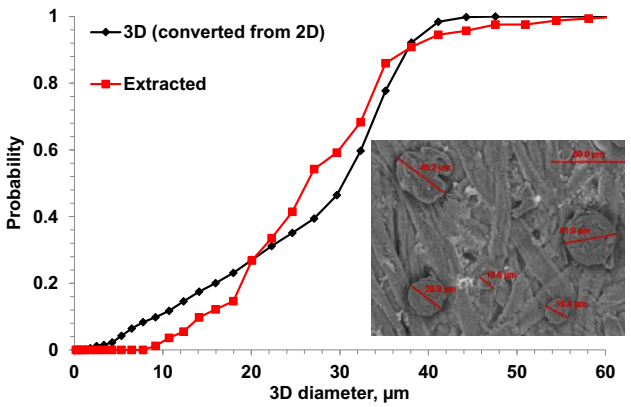

Figure 3. Comparison of diameter distributions of extracted nodules with 3D converted from an automated SEM/EDX analysis of polished section 2D. Insert shows extracted graphite nodules.

In addition to structural reconstruction model, a classical instantaneous nucleation in random space ("ideal") model was used to observe departure of experiment nodule diameter distribution in castings from distribution followed from this model. In this case, particle distribution function [PDF = $P(D)/\Delta D$, where $P(D)$ is a probability of 3D nodule diameter at ΔD interval] was used because the shape of the PDF curve does not depend on particle interval size.

Results

The experimental results are presented in this article for the Mg-treated non-inoculated SGI ("base"), inoculated after that by a commercial inoculant SGI ("inoculant"), as well as for two sets of additions to this inoculant: Set A included primary precipitate forming additions (Zr and Ti) and Set B had additions (S and N) to form mixed and secondary precipitates. For each case, the data present the converted 3D nodule diameter distributions, compared it with the ideal model, the reconstructed solidification kinetics and the family of nonmetallic inclusions located in the matrix and found inside graphite nodules.

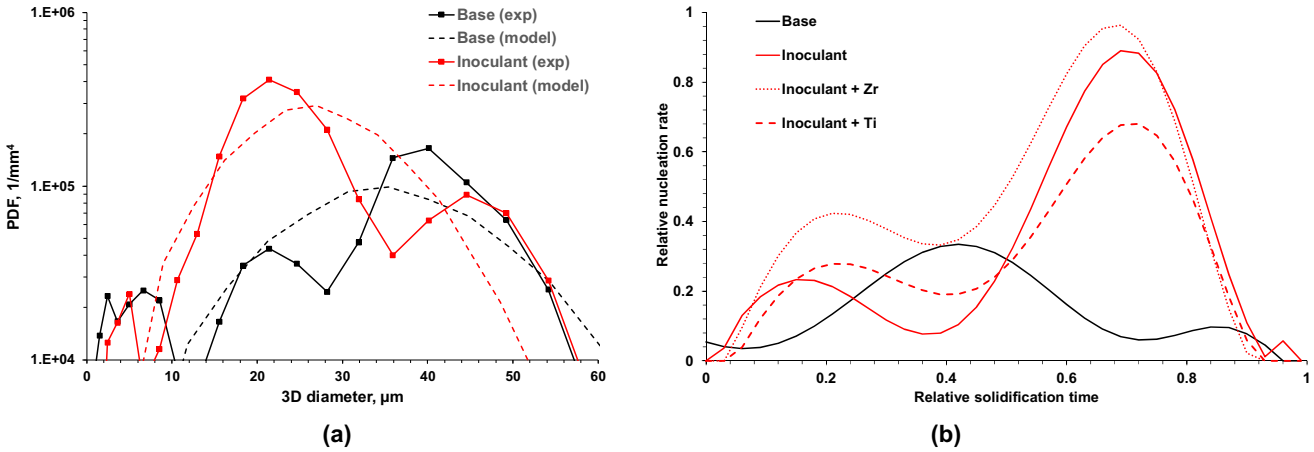

Figure 4. Comparison of experimental and simulated (instantaneous nucleation in random space) particle distribution functions (PDFs) for base and inoculated SGI (a) and reconstructed nucleation rate for base Mg-treated (non-inoculated), inoculated, and treated with Ti- and Zr-addition SGI (b).

Base Mg-Treated and Inoculated SGI

In the base, Mg-treated (not inoculated SGI), the 3D distribution curve of graphite nodule diameters consisted of two distributions: one near normal and an additional set of small nodules. Figure 4a also shows calculated "ideal" nodule distributions for the same as experimental graphite nodules number but assuming instantaneous random nucleation (dotted lines). Inoculation increased the nodule number, decreased an averaged nodule diameter and deformed a distribution curve into three superimposed distributions. Significant departure of an experimental particle distribution curve (PDF_{exp}) from "ideal" model (PDF_{ideal}) in inoculated SGI was observed in both small and large nodule diameters. The relative reconstructed rate of graphite nodule nucleation (Figure 4b) was close to monotonic in the base Mg-treated and consisted of two nucleation waves in inoculated SGI. Here, it is necessary to mention that the nucleation rate was simulated for the remaining melts; therefore, the shapes of both curves (PDF and reconstructed nucleation rate) are different.

The examples of the individual nonmetallic inclusions observed in the base Mg-treated SGI and after inoculation are shown in Figure 5. Shown concentrations of the main elements on this and others SEM/EDX images are given in wt%. Complex Ca–Mg–La–Ce sulfides co-precipitated on early formed prime MgO core were detected inside graphite nodules in inoculated SGI. This precipitation sequence was thermodynamically predicted.

The ternary diagrams, shown in this article, separately present the inclusion family detected in the metal matrix and inside graphite nodules. Figures 6 and 7 show joint ternary diagrams of inclusion families presented in the base, not inoculated Mg-treated and inoculated SGI. Each area on this diagram presents the set of inclusions with three major active elements, and each inclusion is shown only one time. On these diagrams, inclusions in the matrix are presented by its diameter, while nuclei are presented by graphite nodule diameter. There is a visible difference in the nonmetallic inclusion populations located in the matrix versus found inside graphite nodules for both SGI. The

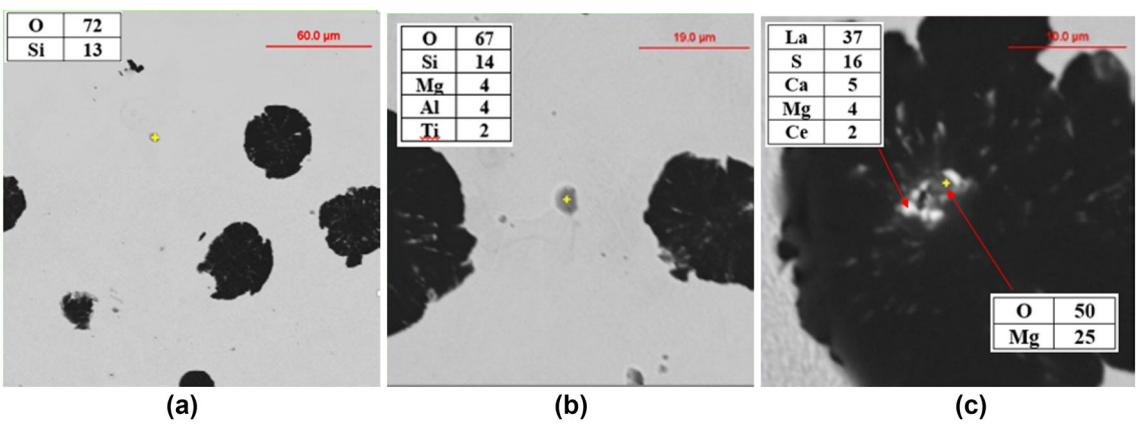

Figure 5. Example of observed nonmetallic inclusions in base Mg-treated SGI (a), after inoculation (b), and (c) complex structure and composition of graphite nuclei.

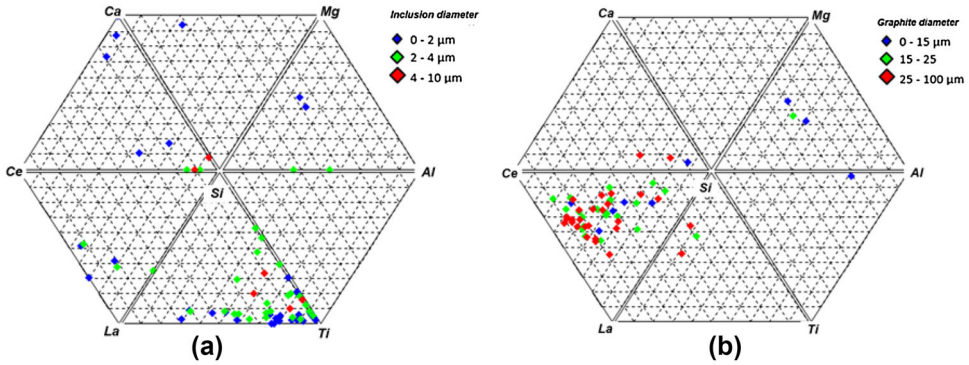

Figure 6. Ternary diagram of nonmetallic inclusions observed in matrix (a) and inside graphite nodules (b) in base (non-inoculated) Mg-treated SGI.

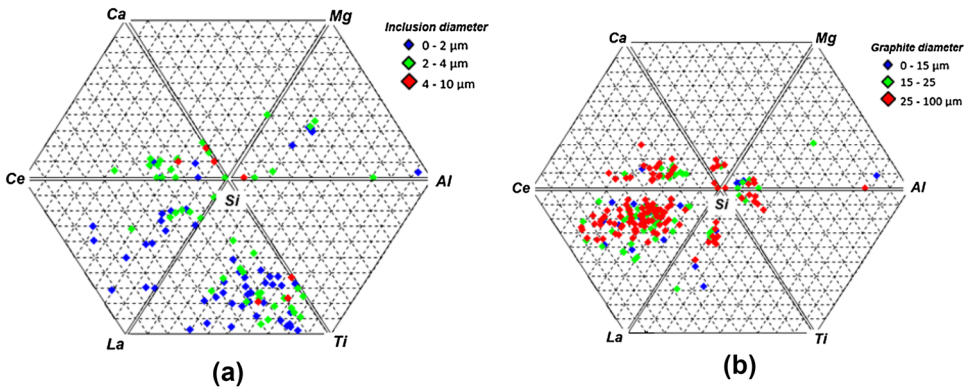

Figure 7. Ternary diagram of nonmetallic inclusions observed in matrix (a) and inside graphite nodules (b) in Mg-treated and inoculated SGI.

results indicate that primary Ce, La and Mg oxides and sulfides which were formed during nodulizing treatment are presented inside nodules, while Ti-bearing inclusions mainly were found in the matrix. The element partitioning between the matrix and graphite nodules can be used as statistical indicator of nucleation activity. Inoculation also increased a variety of Ca- and Si-bearing inclusions involved in nucleation (Figure 7).

An additional analysis was performed to classify inclusions. There are several types of observed inclusions located in the matrix of inoculated SGI which could be considered: the primary large diameter Mg–Si–Ti–La oxides and pure TiN, the secondary small diameter complex Si–Mg–Al nitrides and the mixed (primary and secondary formed) intermediate size Mg–Ca–Ce–La–Ti sulfides (Table 2). Unfortunately, only sulfides and all others types of nuclei (oxides + nitrides) were possible to classify using an automated SEM/EDX analysis in this study because of overlap of specter of light element (Table 3). Ce oxides, La and Mg sulfides and possibly complex Mg–Al–Si nitrides are presented in nuclei family.

Melt Treatment with Primary Inclusion Formers: Zr and Ti

Ti additions slightly decreased while Zr additions increased the 3D number of graphite nodules (N). Zr additions increased a portion of larger graphite nodules in PDF nodule curve, while Ti additions deformed PDF nodule

Table 2. Average Inclusion Compositions by Classes Detected in Matrix of Inoculated SGI (wt%)

Type	D (µm)	Mg	Al	Si	Ca	Ti	La	Ce
Oxides	2.8	12	2	21	5	25	24	8
Sulfides	2.5	13	2	5	6	34	19	2
Nitrides	1.0	25	16	24	–	20	6	2

Table 3. Average Nuclei Compositions by Classes Detected in Inoculated SGI (wt%)

Type	Graphite D (µm)	Mg	Al	Si	Ca	Ti	La	Ce
Others	26	2	6	59	4	3	8	16
Sulfides	22	13	7	41	9	1	18	8

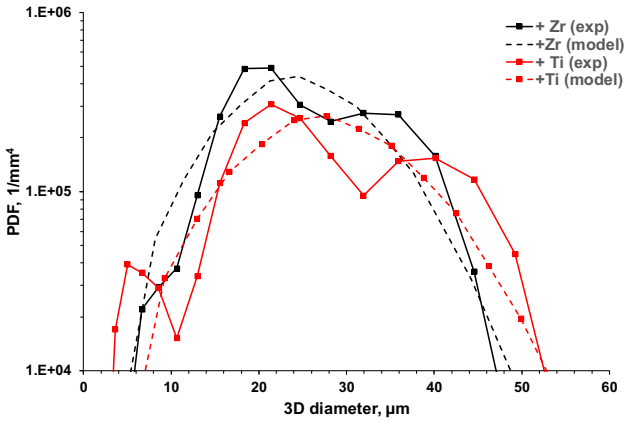

Figure 8. Comparison of experimental and simulated for instantaneous nucleation in random space particle distribution functions (PDFs) for inoculated with Ti- and Zr-addition SGI.

curve in both small and large nodule diameters (Figure 8). The observed transformations of 3D nodule diameter distributions were related to the effect of Zr and Ti on graphite nodule nucleation sequences (Figure 4b). These additions increased the nucleation rate in the early solidification stage.

Adding Zr and Ti with inoculant significantly changed the observed in the matrix and inside graphite nodules nonmetallic inclusions families. SEM image from a backscattered electron detector provided optical contrast of primary pure TiN and complex Ti–Zr nitrides inclusions (dark) and bright Zr–La-bearing inclusions. The ternary diagrams are shown in Figure 9 only for dark inclusions. Inclusion chemistry showed significant differences in inclusion populations with small and large sizes. Small inclusions were abundant in N and Mg in inoculated SGI. This indicates that nitrides formed later upon cooling which is consistent with thermodynamic predictions. Zr and Ti presented in larger quantities in inclusion from SGI treated by these elements.

An example of ternary diagram of nonmetallic incisions found inside graphite nodules in Ti-treated SGI is shown in Figure 10a and comparison of average concentrations of active elements in inclusions from matrix and nuclei presented on diagram (Figure 10b). Zr has a positive partitioning, i.e., concentrated inside nodules, while Ti was rejected from nucleation sites.

Treatment with Mixed and Secondary Inclusion Formers (*N* and *S*)

Figure 11 presents comparison of the 3D graphite nodule diameter distributions and the reconstructed nucleation rate in the inoculated SGI and two alloys treated with S and N additions to inoculant. The S and N additions deformed the shape of graphite nodule diameter distribution curves: (i) even portions of large (30–50 µm) and small (10–30 µm) nodules and (ii) the additional small hubs detected in the range of 1–10 µm. Comparison of an experimental and an "ideal" curve for SGI treated with S addition is shown in Figure 11b. These changes in graphite nodule distributions were related to changes in reconstructed nucleation rate made by S and N additions: (i) increased nucleation rate at the initial solidification period and (ii) provided an additional small nucleation wave at the solidification end.

Adding S with inoculant changed the observed nonmetallic inclusion family. Primary, larger than 2-µm Ca–Mg sulfides were detected in the metal matrix (Figure 12a) and complex-containing La and Ce sulfides co-precipitated on early formed prime MgO core were found inside graphite (similar to shown in Figure 5c). N additions developed, presumably secondary complex Mg–Si–Al nitrides (Figure 13a), precipitated on early formed primary MgO core and served as graphite nodule nucleation sites. S treatment mainly influenced on forming Ce oxides, La sulfides and complex Mg–Ca sulfides located inside graphite nodules (Figure 13b).

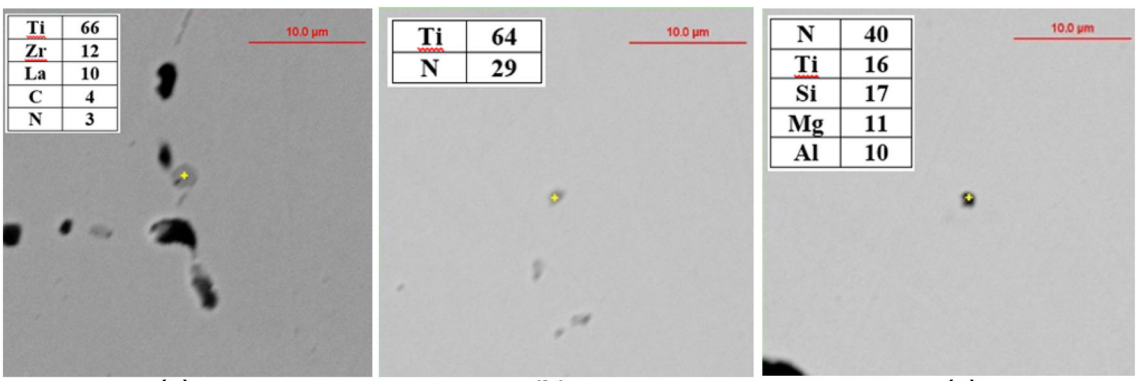

Figure 9. Complex prime Ti–Zr–La carbo-nitride inclusions Zr-treated SGI (a), prime TiN (b) and (c) complex nitride in Ti-treated inoculated SGI found in metal matrix.

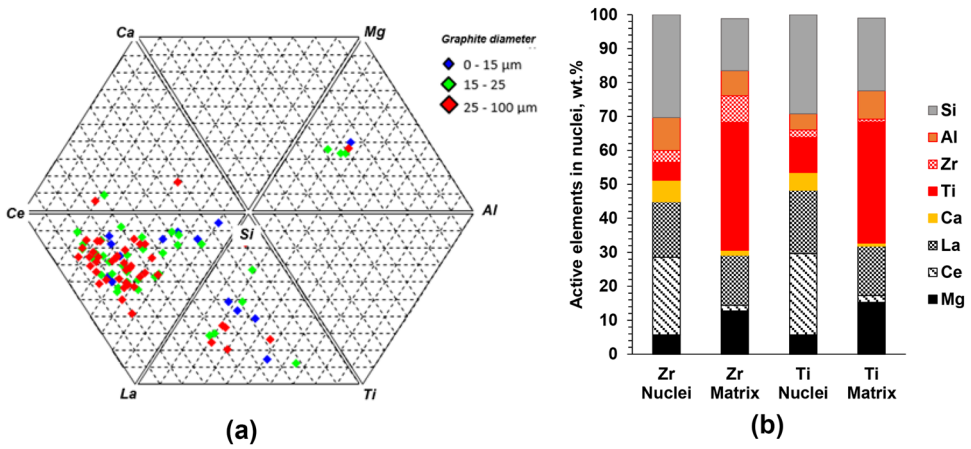

Figure 10. Ternary diagram of nonmetallic inclusions observed inside graphite nodules in Ti-treated SGI (a) and comparison of average active element concentrations in Ti- and Zr-treated SGI (b).

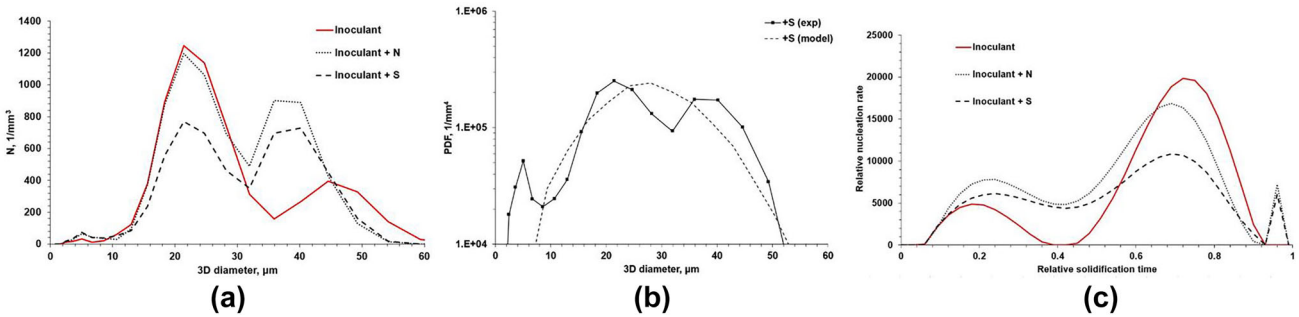

Figure 11. Inoculated SGI and treated with S- and N-addition SGI: (a) 3D graphite nodule size distributions, (b) comparison of experimental and "ideal" particle distribution functions (PDFs) for inoculated with S-addition SGI and (c) reconstructed relative nucleation rate.

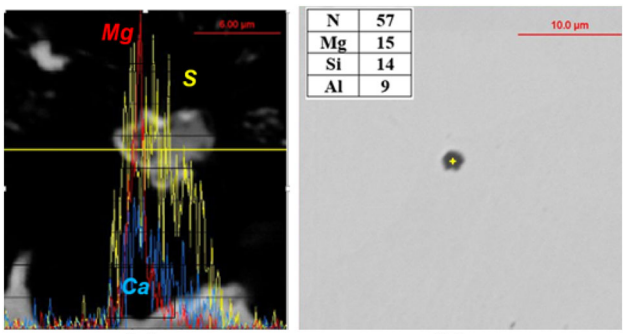

Figure 12. Line scan of prime Ca–Mg sulfide inclusions detected in metal matrix of S-treated SGI (a) and small complex Mg–Si–Al nitride in N-treated inoculated SGI (b).

Discussion: Principles of Engineering Nonmetallic Inclusion to Control Graphite Nodules Nucleation Kinetics in Inoculated SGI

The principles of "Engineering nonmetallic inclusions in SGI" are discussed in this article to describe a methodology for control of solidification of graphite eutectic in SGI by adding the inoculants into the melt that will form the desired:

(a) types of nonmetallic inclusions which have potential to initiate graphite nodules nucleation;
(b) sequence of precipitate formation for prolongation of nucleation events to the solidification end
(c) optimal number, shape and size of these precipitate.

It was shown that thermodynamic simulations of reactions in the melt and during solidification could be used as a first step to select the potential elements and their concentrations. Thermodynamic simulations predicted that the formed precipitates in inoculated SGI could be classified into three classes: (i) existed in the melt before solidification (mainly primary oxides), (ii) formed during solidification as a result of element positive segregation into the remaining melt and decreasing temperature (mainly secondary nitrides), and (iii) intermediate class (mainly sulfides) which could be formed above liquidus as well as in mushy zone. These secondary precipitates (class "ii" and "iii") could promote continuous nucleation and a second

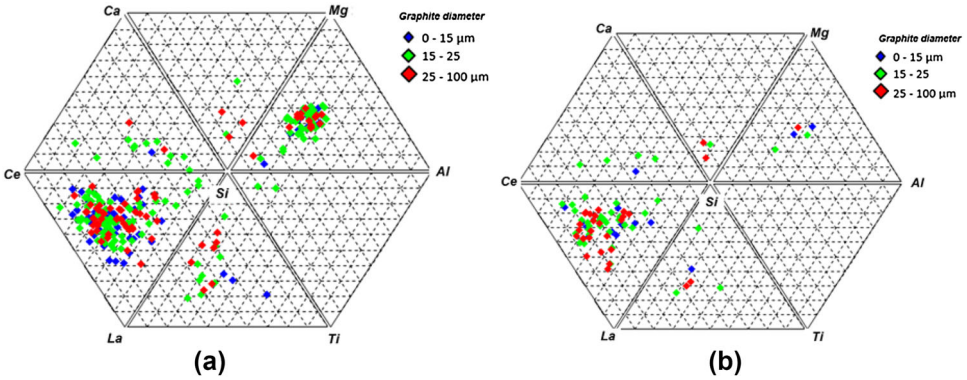

Figure 13. Ternary diagrams of nuclei observed in inoculated Mg-treated SGI with N additions (a) and S addition (b).

nucleation wave of graphite nodules, which was observed in the inoculated castings.

The engineering nonmetallic inclusions can be used for elimination of microporosity and for the other positive outcomes. Table 4 illustrates measured porosity in experimental castings. The experimental results showed that the observed transformations of 3D nodule diameter distribution curves were related to the effect of Zr and Ti on graphite nodule nucleation sequences. These elements promoted nucleation of graphite nodules at an early solidification period which resulted in an increased portion of larger nodules. A moderate improvement in porosity with Zr additions was detected. However, the additions, which form secondary precipitates, can continuously nucleate graphite nodules to the solidification end. This change in solidification sequence was observed in SGI inoculated with S and N additions. Continuous nucleation and the second nucleation waves are practically beneficial for decreasing porosity by small graphite nodules precipitated in inter-dendritic regions.

It is important to note here that optimization of nucleation parameters is still a challenge because of possible negative effects. Extra S additions to inoculant could degrade graphite nodule shape, and large nitrogen additions could promote gas porosity. There is no direct correlation between graphite nodule number and observed porosity in experimental castings. Minor impurity levels in the melt also are very important for development of desired secondary precipitates to control the nucleation kinetics. For example, the formation of the particular Ti or Mg nitrides in the mushy zone will depend on a Ti–Mg ratio (Figure 1b). Also, still a challenge to predict which types of nonmetallic inclusions will have a higher potential to initiate graphite nodules heterogeneous nucleation.

Table 4. Measured Microporosity in Experimental Castings (Middle Bosses). Archimedes Method

SGI	Porosity (%)	Graphite nodule (1/mm^2)
Base	22.8	135
Inoculated	16.0	230
Inoculated + Zr	9.1	290
Inoculated + Ti	17.0	222
Inoculant + N	7.0	263
Inoculated + S	0.5	270

Conclusions

The methodology of engineering nonmetallic inclusions to control nucleation kinetics of graphite nodules based on thermodynamic simulations, an automated SEM/EDX analysis of formed precipitates, and a structural reconstruction of relative solidification kinetics was suggested and tested in inoculated SGI.

It was shown that:

- Zr additions can directly form the potential nuclei in the melt by reactions with dissolved oxygen and nitrogen and initiate heterogeneous nucleation of graphite nodules on early solidification period;
- S and N additions to inoculant can form primary and secondary inclusions precipitated during solidification which stimulate a continuous nucleation and reduce porosity in casting.

Acknowledgement

The authors would like to thank Dr. Mingzhi Xu for help with Magma simulation and Ph.D. student Obinna Adaba to perform graphite extraction. Special thanks to undergrad students Michael Khayt and Stephen Arant for help with experimental heat and sample preparation. This study is a part of AFS project, and author thanks the members of 5R Research Committee for support research and result discussion. Funding was provided by American Foundry Scociety (Grant No. 17-18#01).

REFERENCES

1. P. Kainzinger, C. Guster, M. Severing, A. Wolf: *Proceedings 13th International Conference on Fracture*, Beijing, China (2013)
2. F. Mampaey, Int. J. Cast Metals Res. **11**, 307 (1999)
3. G. Alonso, D.M. Stefanescu, R. Suarez, A. Loizaga, G.G. Zarrabeitia, Int. J. Metal Cast. **27**(2), 87 (2014)
4. A. Knuutinen, K. Nogita, S. McDonald, A. Dohle, J. Light Met. **1**, 241 (2001)
5. T. Skaland, Int. J. Cast Met. Res. **16**(1–3), 11 (2003)
6. K. Solvio, L. Elmquist, Int. J. Cast Met. Res. **26**(4), 220 (2013)
7. G. Lesoult, Int. J. Cast Met. Res. **22**, 2 (1999)
8. M. Chisamera, I. Riposan, S. Stan, M. Barstow: AFS Proceedings, Paper 12-071 (2012)
9. K.M. Pedersen, N.S. Tiedjie, Mater. Charact. **59**, 1111 (2008)
10. S. Lekakh, J. Qing, V. Richards, K. Peaslee, AFS Trans. **121**, 1321 (2013)
11. Y. Yin, Z. Tu, J. Zhou, D. Zhang, M. Wang, Z. Guo, C. Liu, X. Chen, Met. Mater. Trans A **48**(8), 3794 (2017)
12. K. Yamane, H. Yasuda, A. Sugiyama, T. Nadira, M. Yoshita, K. Morishita, K. Uesugi, T. Takeuchi, Y. Suzuki, Met. Mater. Trans. A **46**, 4937 (2015)
13. A. Dioszegi, I. Svensson, Int. J. Cast Met. Res. **18**(1), 41 (2005)
14. C.A. Bhaskaran, D.J. Wirth, AFS Trans. **02–003**, 1 (2002)
15. P. Larranaga, J.M. Gutierres, A. Loizaga, J. Sertucha, R. Suarez: AFS Trans., Paper 08-008 (05), (2008)
16. D.M. Stefanescu, M. Morgan, S. Boonmee, W.L. Guesser: AFS Proceedings, Paper 12-0.45 (2012)
17. S. Lekakh, ISIJ Inter. **56**(5), 812 (2016)
18. S. Lekakh, B. Hrebec, Int. J Metalcasting **10**(4), 389–400 (2016)
19. J. Lacaze, M. Castro, G. Lesoult, Acta Mater. **46**(3), 997 (1998)
20. H. Muhmond, *Doctoral Thesis* (Stockholm, Sweden, 2014)
21. Factsage software, www.factsage.com
22. J.K. Solberg, M.I. Onsoien, Mater. Sci. Tech. **17**(10), 1238 (2001)
23. G. Alonso, D. M. Stefanescu, R. Larranaga, R. Suarez, E. De la Fuente: *AFS Proceedings of the 121st Metalcasting Congress*, Paper 17-031 (2017)
24. S. Lekakh, V. Richards, K. Peaslee, Int. J Metalcasting **3**(4), 25–37 (2009)
25. M. Harris, O. Adaba, S. Lekakh, R. O'Malley, V. Richards: *AISTech Proceedings* (2015), p. 3315